Investigation of double tropopause spatial and temporal global variability utilizing High Resolution Dynamics Limb Sounder temperature observations

Tanya R. Peevey,[1,2,3] John C. Gille,[1,2] Cora E. Randall,[3,4] and Anne Kunz[5]

Received 23 June 2011; revised 7 November 2011; accepted 11 November 2011; published 11 January 2012.

[1] This study examines the seasonal variation of the double tropopause (DT) using data from the High Resolution Dynamics Limb Sounder. The combination of high data density and high vertical resolution available with this satellite instrument allows for the detailed analysis of fine-scale structures such as the DT. The spatial distribution of DT frequency is examined for all seasons from 2005 to 2007. Global analysis of this distribution reveals that DTs have a strong tendency to follow the zonal wind pattern and are present all year over the Andes. Moreover, during Northern Hemisphere winter/spring, there is a 15% decrease in the DT frequency over the eastern Pacific and western Atlantic, two regions of wave breaking produced from a weakening of the zonal flow. Significant DT thickness values are also present over these regions, but are found to extend further poleward than the corresponding frequency pattern. A time series of DT frequencies is analyzed and shows an increase in daily frequencies during 2006 that highlights the interannual variability of this thermal structure. For the first time, DT duration is investigated in the extratropics utilizing a Hovmöller diagram of DT frequency. This representation highlights two preferred regions of formation, the Pacific and Atlantic. The slope of the feature gives it a speed of 18 m/s in the Northern Hemisphere and a slightly faster speed for the Southern Hemisphere. These speeds and the corresponding structures highlight a potential connection between upper tropospheric waves and DTs.

Citation: Peevey, T. R., J. C. Gille, C. E. Randall, and A. Kunz (2012), Investigation of double tropopause spatial and temporal global variability utilizing High Resolution Dynamics Limb Sounder temperature observations, *J. Geophys. Res.*, *117*, D01105, doi:10.1029/2011JD016443.

1. Introduction

[2] The Upper Troposphere Lower Stratosphere (UTLS) region in the Earth's atmosphere plays a critical role in the climate system. The tropopause is a key feature in the UTLS, separating layers with fundamentally different characteristics in static stability [*Hoinka*, 1997], chemical constituents [*Bethan et al.*, 1996] and potential vorticity [*Hoskins et al.*, 1985]. In the region surrounding the tropopause chemical constituents are redistributed through dynamical processes contributing to stratosphere-troposphere exchange (STE), e.g., tropopause folds and the Brewer-Dobson circulation [*Holton et al.*, 1995]. The magnitude of this air exchange is dependent upon the definition of the tropopause (dynamical, thermal/lapse rate, or chemical), since different definitions result in different vertical locations of this boundary [*Bethan et al.*, 1996; *Pan et al.*, 2004; *Wirth*, 2001]. *Wirth* [2001] examined the tropopause-vorticity relationship and found that large differences between the thermal and dynamical (2.5 PVU) tropopause heights are associated with cyclonic circulations. When the thermal definition of the tropopause [*World Meteorological Organization (WMO)*, 1957] is applied during the winter, an active season for intense weather systems, discontinuities, i.e., breaks in the tropopause, are observed at the subtropical jet. At and poleward of these breaks multiple tropopauses or stable layers have been found in the thermal structure of the atmosphere using sounding data [*Seidel and Randel*, 2006]. The synoptic structure of these stable layers has been studied by *Shapiro* [1978] in relation to upper level jet stream-frontal zones using aircraft observations and later defined using potential vorticity and ozone distributions [*Shapiro*, 1980]. Later, *Keyser and Shapiro* [1986] reviewed the structure of upper level frontal zones and illustrated the split in the static stability layer marking the upper tropospheric frontal zone during Kelvin-Helmholtz billows. This relationship has also been discussed and suggested in more recent studies comparing the spatial

[1]National Center for Atmospheric Research, Boulder, Colorado, USA.
[2]Center for Limb Atmospheric Sounding, University of Colorado at Boulder, Boulder, Colorado, USA.
[3]Department of Atmospheric and Oceanic Sciences, University of Colorado at Boulder, Boulder, Colorado, USA.
[4]Laboratory for Atmospheric and Space Sciences, University of Colorado at Boulder, Boulder, Colorado, USA.
[5]Institute for Energy and Climate Research, IEK-7: Stratosphere, Forschungszentrum Jülich, Jülich, Germany.

0148-0227/12/2011JD016443

distribution of multiple tropopauses to the distribution of synoptic features, such as a tropopause fold [*Añel et al.*, 2008; *Schmidt et al.*, 2006].

[3] Even though the DT has been known since the advent of upper air soundings in the 1950s [*Kochanski*, 1955] studies over the past decade have added greatly to scientific knowledge of this thermal structure. Some of these recent studies have quantified the variability and trends of the DT and have shown that a large fraction of temperature profiles form a DT during the midlatitude winter [*Seidel and Randel*, 2006; *Schmidt et al.*, 2006; *Bischoff et al.*, 2007]. *Randel et al.* [2007] expanded upon these studies by examining DT global variability and its relationship to relative vorticity and ozonesonde profiles using radiosonde profiles, reanalysis data, and radio occultation temperature profiles. The authors found that DTs tend to form above strong cyclonic circulation systems and that their formation is accompanied by areas of reduced ozone concentration. Those results support observations which have shown that DTs are found on the poleward side of the jet and suggest enhanced transport from the upper tropical troposphere. *Pan et al.* [2009] studied two intrusions events and analyzed the connection between the development of the secondary tropopause, or DT, and the tropopause break at the subtropical jet using data from the high resolution dynamics limb sounder (HIRDLS) [*Gille et al.*, 2008]. These case studies showed layers of tropospheric air extending beyond the subtropical jet into the lower stratosphere during Rossby wave breaking events. The intrusions contain air of low ozone concentration and low static stability and develop as the layer of tropospheric air forms a DT during the wave breaking. *Homeyer et al.* [2011] expanded upon that work by investigating the development of both the vertical and horizontal structure of the tropospheric intrusion using flight data from the Stratosphere-Troposphere Analyses of Regional Transport 2008 (START08). The authors found, by means of kinematic and chemical diagnostics, that all observed intrusions formed during Rossby wave breaking events and primarily in the Pacific Ocean. Moreover, during large events the transported air can separate from its tropical reservoir and mix with the background stratosphere air. Consequently, the DT could be used to identify areas of transport and possible mixing that result in the redistribution of chemical constituents in the UTLS. This redistribution has global importance because when it is irreversible it results in mixing that can change the UTLS trace gas composition, e.g., O_3 or H_2O, and has the potential to affect surface climate [*Forster and Shine*, 1997; *Solomon et al.*, 2010].

[4] The previously mentioned studies have shown that DTs can form during Rossby wave breaking [*Pan et al.*, 2009; *Homeyer et al.*, 2011], prefer upper level cyclonic circulations [*Randel et al.*, 2007], and occur more frequently in regions of enhanced synoptic activity [*Añel et al.*, 2008]. This evidence prompted *Wang and Polvani* [2011] to investigate the role of baroclinic eddies in the formation and maintenance of the DT using a model. They found that DT formation could not be simulated without representing the Tropopause Inversion Layer (TIL) [*Birner et al.*, 2002; *Birner*, 2006] in the model. The authors found this relationship difficult to understand since the seasonal cycle of the DT and the TIL are nearly opposite. Furthermore, the study found that air masses within the DT originate from high latitudes, contradicting results put forward by *Pan et al.* [2009]. These recent studies highlight that the formation and maintenance of the DT is still not completely understood and that there is still a need to investigate the mechanisms behind its formation.

[5] The goal of this study is to further understand the characteristics of DT formation by analyzing its spatial patterns using high spatial resolution temperature data from HIRDLS and relating the results to other atmospheric processes, such as wave breaking. HIRDLS generates a large data set with global coverage and high spatial resolution of 1 km in the vertical and 100 km along track. Previous studies examining spatial patterns and DT characteristics [e.g., *Schmidt et al.*, 2006; *Añel et al.*, 2008] have used data sets with a vertical resolution equivalent to or better than that available with HIRDLS. However, those data sets do not have the spatial resolution or data density of HIRDLS. For example, the Challenging Minisatellite Payload (CHAMP) and Satélite de Aplicaciones Cientificas-C (SAC-C) data sets used by *Randel et al.* [2007] and *Schmidt et al.* [2006] only provide 150–200 profiles per day per antenna. Additionally, other studies have used radiosonde data [e.g., *Añel et al.*, 2008; *Randel et al.*, 2007] that, despite their very high vertical resolution, have large gaps in data coverage that can occur over both the continents and the oceans. HIRDLS observes ~5500 profiles per day with no large gaps in data coverage and with a large amount of data, ~400 profiles, in each 3° × 15° latitude-longitude bin. These features allow for the analysis of horizontal structure not seen with previous instruments.

[6] Details on the three data sets used in this study can be found in section 2. The application of the lapse rate definition of the tropopause is described in section 3, along with an example of its implementation and any additional restrictions. Other methods, such as binning techniques, are also described here. Results are presented in section 4 with the following subsections: seasonality, thickness, and interannual variability of the DT. Implications of the results are discussed in section 5 and then summarized in section 6.

2. Data Description

2.1. HIRDLS Level 2 Profiles

[7] The HIRDLS Instrument is a 21 channel infrared limb scanning radiometer. It is one of four instruments onboard the NASA EOS-Aura satellite, which was launched 15 July 2004 into a sun-synchronous polar orbit with a period of 99 min. At an altitude of 705 km, the satellite orbits ~15 times per day, with a longitudinal separation of 24.75° between orbits and an along track separation of ~75–100 km or ~1° between profiles. HIRDLS measures ~5500 profiles per day and passes the equator twice per orbit, once at ~00:00 and once at ~15:00 local time in a latitude range of approximately 63°S to 80°N. The asymmetry in the equator passing times is a result of the Kapton blockage forcing HIRDLS to look 47° to the side of the satellite orbit track [*Gille et al.*, 2008; *Gille and Gray*, 2011]. Therefore the local time at the measurement locations are earlier/later for the descending/ascending orbit. HIRDLS data collection began on 21 January 2005 and ended in early 2008 when the optical chopper failed. Data is gathered by measuring emission from the Earth's atmosphere in the infrared, between

6 and 18 μm ($\sim$550–1670 cm^{-1}), which allows for near-global coverage day and night. Temperature measurements calculated from the CO_2 bands between 15 and 17 μm are used for locating both single and double tropopauses. (Detailed information on version 3 and the validation of the temperature product can be found in the work of *Gille et al.* [2008]). The present study utilizes altitude and temperature data from version 5 [*Gille and Barnett*, 2010], a recently available version, in the analysis of the thermal tropopause and its variability. Altitude is calculated by the Science Data Processing Toolkit Geolocation Package using satellite instrument ephemeris and altitude data with pointing information. This altitude data is only used when calculating differences in altitude for the lapse rate equation and for DT thickness values, thus removing any systematic errors that may be present. More information on the Toolkit can be found in the work of *Noerdlinger and Klein*, [1995]. Information regarding the HIRDLS retrieval algorithm can be found in the work of *Khosravi et al.* [2009].

[8] HIRDLS can reproduce the atmospheric temperature structure in both the horizontal and vertical, agreeing well with radiosondes, lidar, ACE-FTS and ECMWF [*Gille et al.*, 2008; *Gille and Barnett*, 2010]. A key attribute of this instrument is its high vertical resolution [*Gille et al.*, 2008; *Barnett et al.*, 2008; *Gille and Barnett*, 2010; *Wright et al.*, 2011]. The resolution is $\sim$1 km and is consistent from the upper troposphere to the lower mesosphere. This makes HIRDLS an effective instrument for measuring fine atmospheric features in the UTLS, a difficult region to measure with previous satellites [*Lahoz et al.*, 2007; *Olsen et al.*, 2010]. Additionally, high spatial resolution measurements provided by HIRDLS offer a unique opportunity to examine atmospheric features that can have an extensive meridional structure, such as the DT. HIRDLS temperature observations are analyzed starting from 29 January 2005, when reliable data collection began.

2.2. HIRDLS Gridded Data

[9] A HIRDLS Gridded data set is used to improve the analysis of the duration and motion of the double tropopause, since spatial and temporal continuity is required, a characteristic that is not available with raw satellite observations. This data set was created following the suggestion of *Rodgers* [1976, 2000] to use a Kalman filter as a sequential estimator. The HIRDLS scan track crosses each latitude within its range twice: once on the ascending (mostly day) segment of the orbit, and also on the descending segment, resulting in $\sim$29 crossings each day. Retrieved profiles within a 2° band are treated as a time series. Here, as in the work of *Kohri* [1981] and *Remsberg et al.* [1990], the field at each latitude and pressure level is represented as a mean plus coefficients of the sine and cosine components of the first 6 zonal waves, for a total of 13 time-varying coefficients.

[10] In the sequential estimation, the next retrieved value is combined with the previous estimate at the new measurement location, each weighted by its error. (In the case of the previous estimate, the error determined at the previous step must be increased to account for the growth in uncertainty since the last determination.) This results in a new vector of coefficients and a matrix of their covariances. By carrying out this estimation going both forward and backward in time, and combining the results, each estimate is both smooth and continuous in time, reflecting both previous and subsequent observations. Estimates of the values at synoptic times are obtained by interpolating between the estimates at the measurement times. This allows for conversion of the asynoptic measurements into objectively analyzed synoptic fields. In general the gridded fields agree with the retrievals to within the retrieval precision. *Kohri* [1981] and *Remsberg et al.* [1990] show examples of the fidelity of the gridded fields to the input data and their ability to accurately estimate daily planetary wave characteristics.

[11] In the application to be described later, values were calculated on a 2° $\times$ 4° latitude by longitude grid. Clearly there is no information on scales smaller than wave number 6. In this application, the Kalman filter estimator is an effective, convenient, and objective way to interpolate the data in space and time.

2.3. GEOS-5.1.0

[12] Goddard Earth Observing System Model, Version 5 (GEOS-5) systems have been developed at the Global Modeling and Assimilation Office (GMAO) using a combination of model forecasts and observations [*Rienecker et al.* 2008]. GEOS-5.1.0 is specifically used in this study since it is one of the newest assimilation systems from GMAO and offers high vertical resolution in the UTLS, a property not available with older assimilation models. Furthermore, GEOS-5.1.0 was developed to support the Aura mission and NASA Earth science research. Last, seasonal zonal wind patterns shown in this manuscript agree with previous studies [*Kunz et al.*, 2011; *Nakamura*, 1994], supporting the reliability of the wind product. GEOS-5 zonal wind speed data interpolated onto the 200 hPa pressure surface are used in this study to supplement DT plots with information pertaining to the dynamics of the atmospheric feature. This pressure surface, also used by *Randel et al.* [2007], is chosen because it is typically near the core of the jet.

[13] GEOS-5.1.0 spans 5 years, October 2003 to 2008 and offers four analysis windows (00:00, 06:00, 12:00, and 18:00 UT) that provide either an instantaneous field (no time averaging) or 6 h time-averaged field time-stamped at the center of the averaging window depending on the variable of interest. Both the wind data used to supplement this study and the temperature data used as HIRDLS a priori are 6 h time averaged fields. The horizontal resolution of this version is 1/2° latitude by 2/3° longitude. Vertically, the GEOS-5 version used in this study offers 72 model levels, running from the surface to 0.01 hPa, with a vertical resolution of $\sim$1 km at the tropopause [*Rienecker et al.* 2008].

3. Methodology

3.1. Approach

[14] The DT is identified using the WMO thermal definition [*WMO*, 1957]: (1) The first tropopause is defined as the lowest level at which the lapse rate γ (defined as $-dT/dz$) decreases to 2 °C/km or less, provided also the average lapse rate between this level and all higher levels within 2 km does not exceed 2 °C/km; (2) If above the first tropopause the average lapse rate between any level and all higher levels within 1 km exceeds 3 °C/km, then a second tropopause is

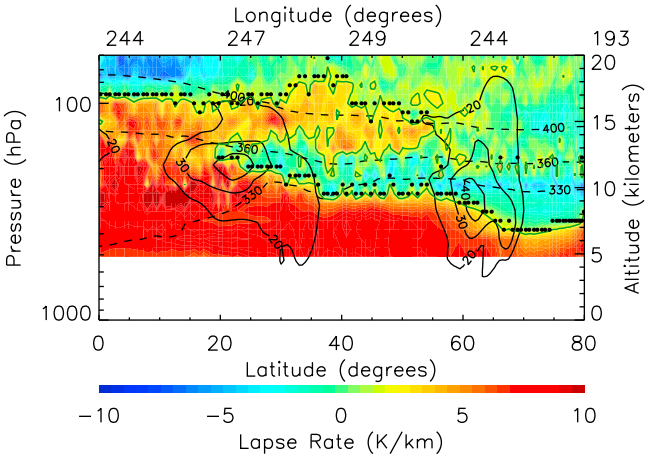

Figure 1. Cross section along the HIRDLS scan track, at 08:00 UTC on the 26 January 2006, of lapse rate calculated from HIRDLS temperature observations. Superimposed is the location of the tropopause (black filled circles), the 2°C/km WMO criterion (green contour), zonal wind (solid black contour), and the potential temperature (dashed black contour). Zonal wind contours are 20 m/s, 30 m/s, and 40 m/s. Potential temperature contours are 330 K, 360 K, and 400 K.

defined by the same criterion as under (1). The second tropopause may be either within or above the 1 km layer discussed in step 2. To clarify these criteria and their implementation the basic logic of the algorithm developed for this study is outlined in Appendix A.

[15] The algorithm is applied to both the HIRDLS Level 2 profiles and the HIRDLS Gridded data with the following restriction. The lapse rate for each profile is calculated at and above altitudes of 5 km, or ~550 hPa, to avoid false readings produced by boundary layer inversions. No additional restrictions are implemented such as eliminating temperatures below cloud top. Therefore, temperature observations used in this analysis are not cloud cleared and include, by construction of the optimal estimation method, a priori contributions that become progressively larger below the cloud top [*Khosravi et al.*, 2009]. A priori data used in the HIRDLS retrieval process are from GEOS-5.1.0 and levels with a priori contributions are included in the analysis for three reasons. First, comparisons with GEOS-5 conducted within the HIRDLS team have shown good agreement between the two data sets above clouds, where there are no contributions from a priori. This result points to the high likelihood of agreement between HIRDLS and GEOS5 below cloud tops and thus the confidence in GEOS5 to reasonably represent HIRDLS in that region. Second, case studies comparing NCEP and HIRDLS have been conducted by the authors and also show good agreement above 5 km. Third, excluding levels below the cloud top from the analysis does not change the spatial structure, only the magnitudes, of the seasonal features shown in the results section.

[16] Additionally, analysis is restricted to a latitude range of 60°S–60°N instead of spanning the full range available, 63°S–80°N, for three reasons. First, HIRDLS orbits switch from a North-South orientation to an East-West orientation and the feature of interest in this study, the DT, usually has a North-South orientation. Additionally, this change in orientation greatly increases the number of profiles per bin, resulting in geometric affects that could produce unrealistic increases in DT frequency in these regions. Second, the thermal tropopause is not appropriate during the polar winter due to the isothermal nature of the atmosphere in this region [*Zängl and Hoinka*, 2001; *Pan and Munchak*, 2011]. Third, the influence of the TIL, a feature which increases in thickness toward the poles, on the DT is still not fully understood [*Wang and Polvani*, 2011]. Additional criteria would need to be added to the DT algorithm to accurately find the thermal tropopause in these regions. However, such an analysis is beyond the scope of this study, which focuses on midlatitude DTs that extend from the subtropical jet. Lastly, the algorithm does not search for the third tropopause since its occurrence frequency is less than 20% in the winter [*Randel et al.*, 2007] and is outside the UTLS region, which is the focus of this study.

[17] Multiple figures in this manuscript represent DT information using bins and therefore, a brief description of the binning and normalization process is warranted. These figures are generated by first counting the number of profiles with a DT and placing this data into the corresponding 3° × 15° latitude-longitude bin. Next, the quantities in each bin are divided by the total number of profiles in their bin. This normalizing factor accounts for the variation of the number of profiles in each bin which averages around 400 profiles for each season and is approximately constant within the analyzed latitude range. These calculated DT frequencies are used in section 4.2 to remove DT profiles that correspond to frequency values greater than 15%. This filtering technique, also used by *Randel et al.* [2007], is implemented for these figures to focus the analysis on individual synoptic structures and not waves, such as equatorial waves, that slightly perturb the local stability profile.

3.2. Identification

[18] The WMO tropopause definition is applied to the HIRDLS data using the previously discussed algorithm. Multiple days in the spring of each year are found to show a poleward intrusion of tropospheric air extending from the subtropics to the extratropics, highlighting the laminar nature of the intruding air. As an example, the lapse rate on 26 January 2006 is shown in Figure 1. This day is shown since the spatial extent of this event is significant and well defined, thus clearly outlining the structure of the DT.

[19] This event occurs at approximately 08:00 UTC and is located over the eastern section of the Pacific Ocean at approximately 248° longitude. The DT feature is indicated with black dots and the GEOS-5 zonal wind with black contours. The black dots clearly highlight a tropospheric intrusion, with the DT extending from the subtropical jet/~20°N toward higher latitudes ending at the polar jet/~55°N. The full shape of the intrusion is highlighted using a green contour, representing the 2 °C/km lapse rate line. In Figure 1 the poleward intrusion contains air with a lapse rate greater than 2 °C/km, thus air of low stability which indicates that it is tropospheric (not stratospheric) in nature. The layer of air below the poleward intrusion, the lower lamina, contains air

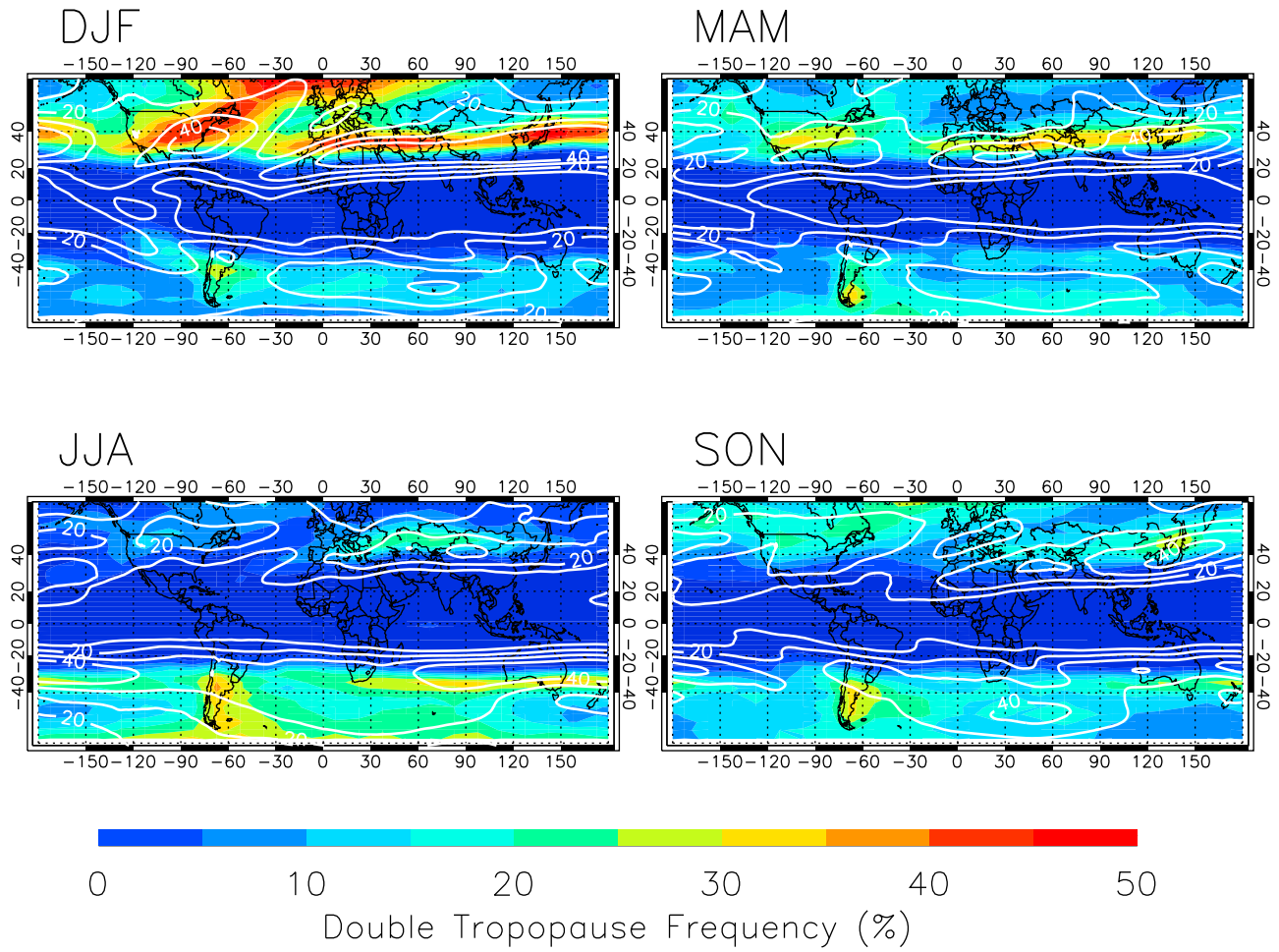

Figure 2. Double Tropopause Frequency of Occurrence obtained using HIRDLS Level 2 data. Plot shows data from 2005 to 2007 and for all four seasons, (top left) December–January–February (DJF), (top right) March–April–May (MAM), (bottom left) June–July–August (JJA) and (bottom right) September–October–November (SON). Frequencies in each 3° latitude × 15° longitude bin represent the percentage of profiles with a double tropopause. The seasonal mean zonal wind (solid white lines), on the 200 hPa pressure surface, is plotted over the filled contours with the following levels: 10 m/s, 20 m/s, 30 m/s and 40 m/s.

with a lapse rate less than 2 °C/km, thus air of high stability which indicates that it is more stratospheric in nature.

4. Results

4.1. Seasonality

[20] Figure 2 displays the seasonal spatial distribution of DT frequency, which highlights seasonal variation of the DT and preferred regions of formation. The spatial distribution of the DT frequency of occurrence is calculated and mapped using the binning method described in section 2.1. The seasonal mean zonal wind structure, represented with gray contour lines, is generated using GEOS-5 zonal wind data and agrees well with the climatological mean of the jet stream that has been shown in other studies [*Kunz et al.*, 2011; *Schmidt et al.*, 2006]. Four seasons are shown in this figure and labeled according to the months that are analyzed, where DJF represents December–January–February, MAM represents March–April–May, and so on.

[21] In general, DT frequencies are maximum/minimum during the winter/summer in both hemispheres due to the strong winter/weak summer atmospheric circulations, such as cyclonic circulations [*Randel et al.*, 2007]. Additionally frequencies are concentrated at and around the subtropical jet, with maximum frequencies slightly poleward of the jet. This is an expected relationship since the tropopause break is known to form slightly poleward of the subtropical jet core [*Pan et al.*, 2004]. Additionally, it is clear that the Northern Hemisphere reaches a higher winter maximum in DT frequency than that of the Southern Hemisphere. This could be a result of differences in the homogeneity of the land-sea distribution in each hemisphere [*Schmidt et al.*, 2006] that, due to an increase in the land area and the number of extensive mountain ranges, enhances the propagation of topographically forced planetary waves in the Northern Hemisphere [*Holton*, 2004].

[22] During the Northern Hemisphere winter/DJF (Figure 2 (top left)) there is a band of high DT frequencies between

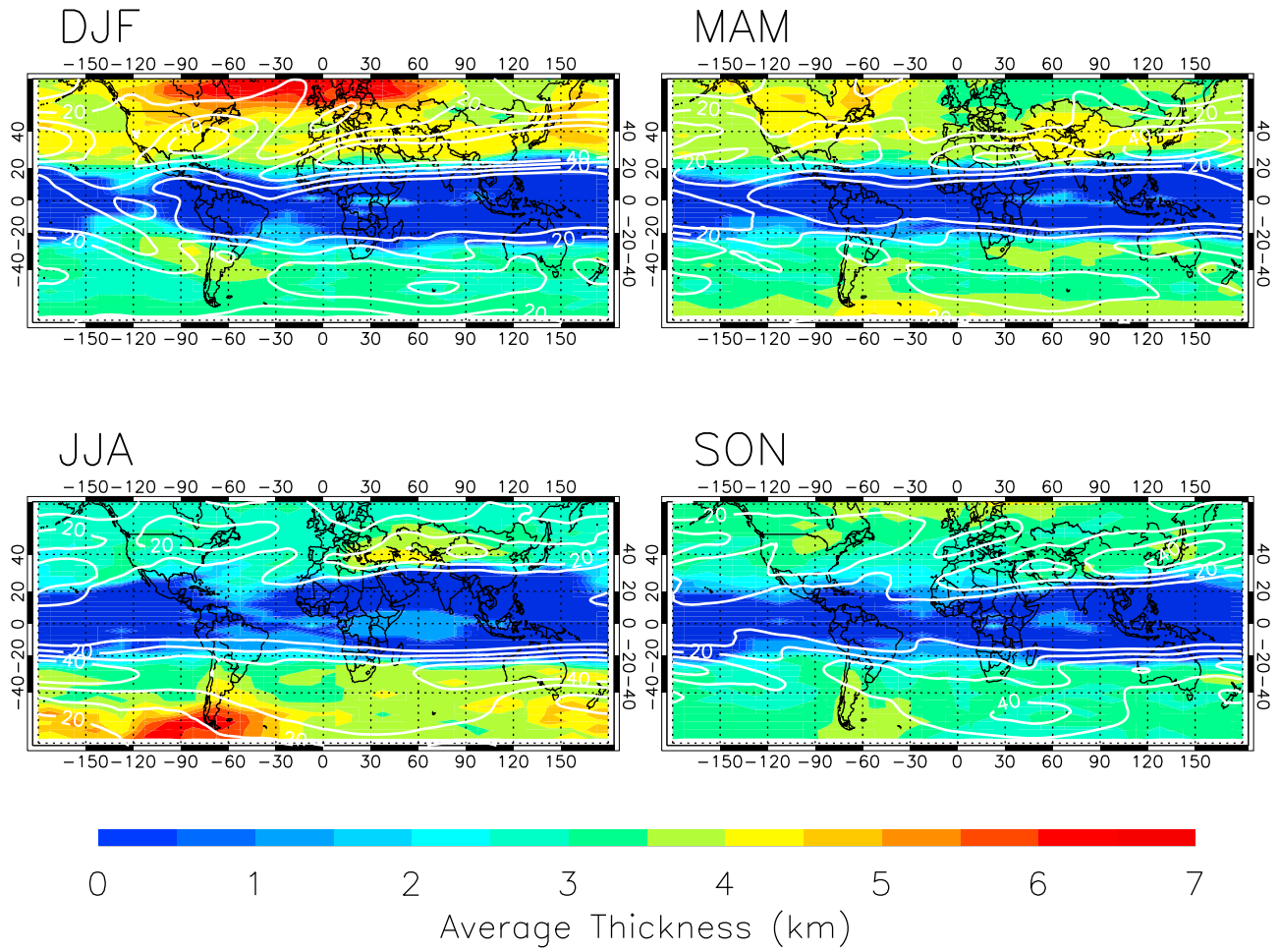

Figure 3. Double Tropopause Thickness obtained using HIRDLS Level 2 data. Plot shows data from 2005 to 2007 and for all four seasons. Thickness is found by calculating the difference in height between the second (highest in altitude) and first (lowest in altitude) tropopause of a DT and then finding the median value of thickness data within each 3° latitude × 15° longitude bin. The seasonal mean zonal wind (solid white lines), on the 200 hPa pressure surface, is plotted over the filled contours with the following levels: 10 m/s, 20 m/s, 30 m/s and 40 m/s.

25°N and 55°N latitude that vary between 40% and 50%. This value decreases to 25% or 30% in the eastern Pacific and central Atlantic, creating two clear breaks that are coincident with minima in the season mean zonal wind and regions of diffluence [*Nakamura*, 1994]. Additionally, frequencies are high over the United States and western Atlantic and follow the tilt in the seasonal jet structure. Poleward of the United States DT frequencies decrease slightly, with a decrease in the zonal wind speed, but then return back to the previous value of ∼40% or ∼45% around 58°N. This high latitude feature extends everywhere except over East Asia and Alaska.

[23] The above mentioned regions of high DT frequency are also present in MAM but decrease in magnitude and shift poleward, matching the seasonal change in the zonal wind. Moving into the summer/JJA, DT frequencies decrease everywhere in the Northern Hemisphere except over the Asian continent where frequencies reach a maximum at approximately 45°N latitude and 60°E longitude and stretch from Eastern Europe to Mongolia. This activity is located just poleward of the Tibetan plateau, a region of westerly flow that is itself on the poleward flank of the Asian monsoon anticyclone.

[24] In the Southern Hemisphere DT frequencies are zonally symmetric with a range of 15%, which is about half the range seen in the Northern Hemisphere. Frequencies are highest during the winter/JJA, located between 25°S and 45°S, and follow the seasonal mean zonal wind pattern as shown by the gray contour lines in Figure 2. Moreover, magnitudes decrease slightly over the southern tip of Western Australia, the eastern Pacific Ocean and the western Atlantic Ocean. Even though these breaks can be subtle they, along with regions of DT frequency maxima, follow the seasonal wind pattern and are regions of poleward Rossby wave breaking [*Peters and Waugh*, 2003]. There is an exception to this relationship over the Andes mountain range in South America where DT frequencies remain high, relative to the rest of the Southern Hemisphere, throughout the year.

4.2. Double Tropopause Thickness

[25] Variations in DT thickness, defined as the altitude difference between the second and first tropopause, are

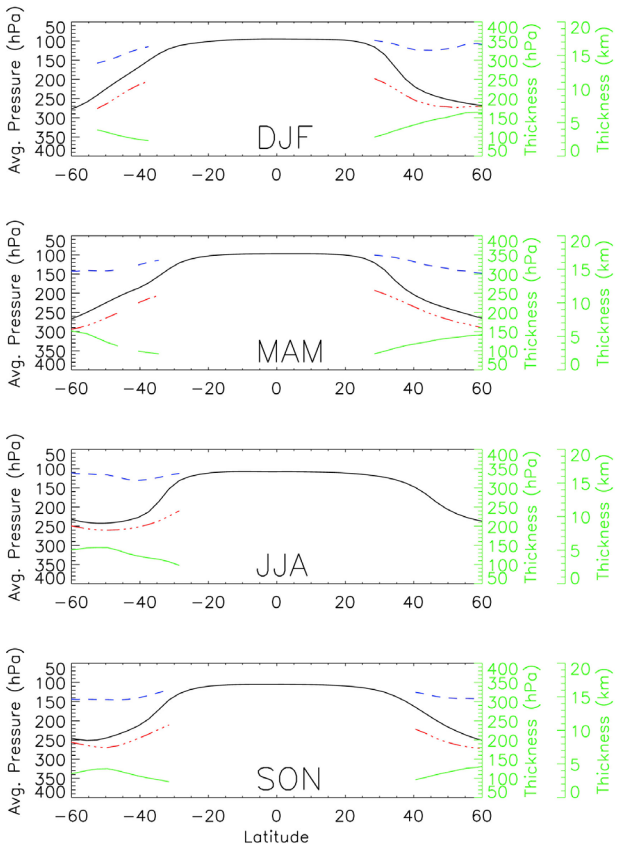

Figure 4. Latitudinal variations in the average pressure of the first and second tropopause within the HIRDLS Level 2 data set. Data is averaged over 3° latitude bins and plotted for all four seasons. Lines on each plot represent the average height of the tropopause when the profile has no double tropopause (solid black line), the average height of the first tropopause when there is a double tropopause (dash-dot-dash red line), the average height of the second tropopause when there is a double tropopause (dashed blue line) and the difference, in hectopascals and kilometers, between the first and second tropopause when there is a DT (solid green line).

analyzed for all four seasons and shown in Figure 3. Results in this figure are produced by finding the average DT thickness for each latitude-longitude bin. For this calculation the median is used as an estimate for the center of the distribution rather than the mean because the distribution of each bin was found to be positively skewed, thus making the median a better estimate. A global plot of DT thickness using the mean is also generated (not shown) and found to show the same general increase in thickness with latitude but without most of the zonal structure seen in Figure 3. In general, DT thicknesses in Figure 3 increase with latitude and vary between 3 and 8 km, reaching a minimum during the late summer and maximum in the late winter in both the Southern and Northern Hemisphere. Additionally, all four graphs in that figure display a spatial structure that resembles the patterns seen in Figure 2.

[26] During DJF DT thicknesses are high, ~4–5 km, over most of the Pacific Ocean (a region of poleward wave breaking [*Peters and Waugh*, 1996]), thus extending beyond the spatial limits of the corresponding frequency pattern. The two patterns continue to overlap into MAM, but also show some deviation over the U.S. and eastern China where high DT thickness values are present farther poleward than DT frequency values. In JJA high thicknesses are present poleward of the Asian anticyclone, which coincides with the DT frequency pattern seen in Figure 2. During SON there is very little structure in either the Northern or Southern Hemisphere. In the Southern Hemisphere a pattern in the thicknesses is only visible, in a substantial way, during JJA. During this season high DT thicknesses are present over and west of the southern tip of South America and poleward of eastern Australia; with the last two features overlapping regions of low DT frequency instead of high DT frequency.

[27] One caveat to consider when examining Figure 3 is the WMO definition itself. That definition places a 2 km restriction on the lapse rate above the first tropopause and, consequently, places a 2 km minimum on the distance between the first and second tropopause. Therefore, regions with thickness values below 2 km are not analyzed and are eliminated from the picture in Figure 4 using the frequency criteria already presented in section 3.1.

[28] Figure 4 is generated to understand the vertical variations in the first and second tropopause and their contribution to latitudinal variations in DT thickness. The seasonal mean pressure levels for the tropopause are shown in Figure 4 and clearly shows the descent of the first tropopause (red line) and the almost constant position of the second tropopause (blue line) when there is a DT in the temperature profile. Additionally, the single tropopause remains between the first and second tropopause of the double tropopause throughout the extratropics. Figure 4 indicates that when there is a DT its thickness generally increases as the pressure/altitude of the first tropopause increases/decreases with latitude. Thus, DTs are thickest toward the poles and smallest toward the tropics, with the strongest gradient occurring just poleward of the STJ during the winter/spring season. In the winter/spring extratropics of each hemisphere DT thickness vary between 4 and 7 km, as shown in Figure 4 (green solid line) and pressure thickness, also the green solid line in Figure 4, varies between 100 and 150 mb.

[29] Results presented so far have focused on seasonal characteristics. This type of an analysis can smooth out the instantaneous behavior of the DT since its position and horizontal size varies on a daily basis. Therefore, the next set of results looks at daily variations in DT frequency from year to year.

4.3. Interannual Variability

[30] Daily DT frequencies, shown in Figure 5, are generated for both the Northern and Southern Hemisphere and for the whole HIRDLS mission by focusing on DTs between 25° and 55° latitude. This latitude range focuses the analysis on features at and poleward of the subtropical jet, since case studies have shown that the DT propagates along the jet stream [*Pan et al.*, 2009] and can be transported poleward [*Homeyer et al.*, 2011]. The quantity plotted in Figure 5 represents the daily percentage of profiles that contain a DT. All three time series in figure exhibit interannual variability with both low- and high-frequency patterns. The high frequency variability was tested since it could be a product

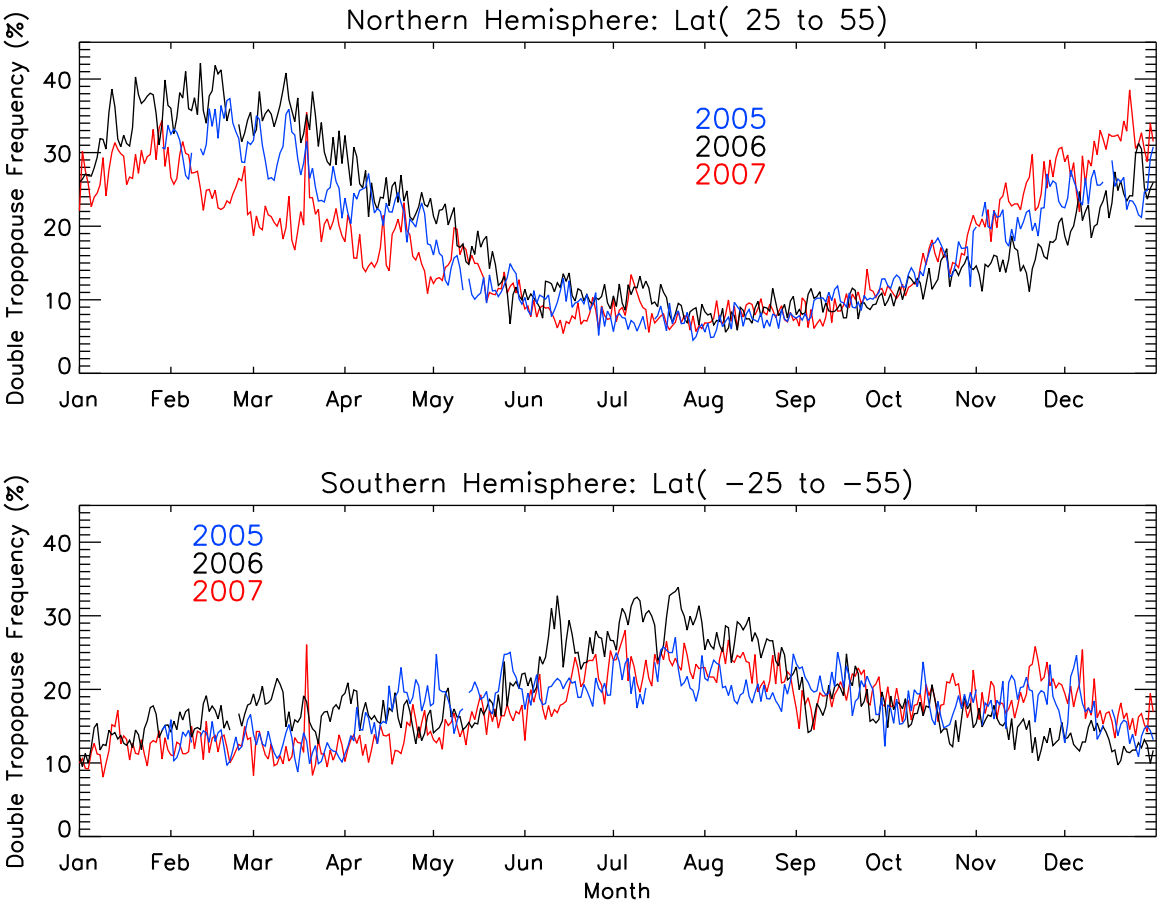

Figure 5. HIRDLS DT daily frequency of occurrence obtained from the Level 2 data and plotted for both the (top) Northern and (bottom) Southern Hemisphere during 2005 (blue), 2006 (black), and 2007 (red). The above plot is obtained by dividing the number of profiles that contain a double tropopause by the number of total profiles, for each and within each 3° latitude bin. No data are available before 21 January 2005 and analysis begins on 29 January 2005.

of data sampling. A time series plot of DT daily frequency was generated using ERA-Interim data (not shown) and compared to Figure 5. The comparative analysis shows that the variability in the ERA-Interim data is very similar to Figure 5 in both the high and low-frequency spectrum. Furthermore, the increase in the number of daily DTs during the winter of 2006 shown using HIRDLS data is also present in ERA-Interim.

[31] Certain features in Figure 5, such as the general seasonality of DT frequency and the large range of frequency values in the Northern Hemisphere relative to the Southern Hemisphere, were also seen in Figure 2. However, Figure 5 contains additional information that clearly highlights the year to year variability of DT frequency and, consequently, characteristics that are not visible with the previous figures. In this plot DT frequency is highest during the winter of 2006 in both the Northern and Southern Hemispheres. Additionally, DT frequency is lowest in the winter during 2007 in the Northern Hemisphere and during both 2005 and 2007 in the Southern Hemisphere. Even though some of these variations seem clear the statistical significance of the variability is tested for both hemispheres using the F test. First the data is tested for normality, once the seasonality is removed, and is found to be normally distributed. Results from the F test for the Northern Hemisphere reveal that the difference between 2005 and 2006 is slightly significant, i.e., p-value ≈ 0.05. Furthermore, the F test also shows that the difference between 2007 and the other two years is very significant, i.e., p-value $\ll 0.05$. For the Southern Hemisphere differences between all three years are found to be statistically significant. This prompts further investigation into this pattern, which begins by first looking at how the daily DT frequencies vary both in latitude and longitude.

[32] First, the daily latitudinal variation of DT frequency is presented and examined. In Figure 6, the filled colored contours represent HIRDLS DT frequencies and the black contours represent GEOS-5 zonal wind speeds interpolated onto the 200 hPa pressure surface. The zonal wind speed is plotted every 5 days instead of daily since synoptic scale representation is sufficient for highlighting the general wind structure. A figure similar to Figure 6 has also been presented by *Schmidt et al.* [2006], but without the added wind information as shown in this manuscript. This additional information draws attention to the DT frequency seasonal pattern and its tendency to coincide with the position of the mean zonal wind, i.e., the seasonal position of the subtropical jet [*Holton*, 2004], in both hemispheres and over all three years. Additionally, the winter to summer poleward

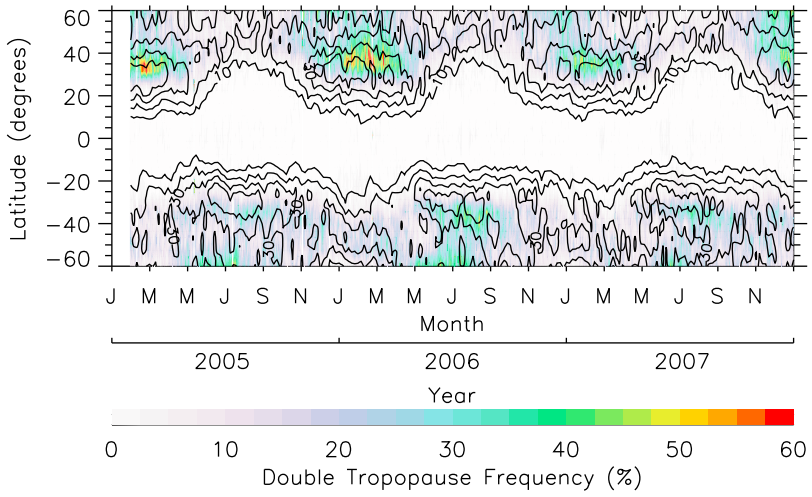

Figure 6. Time series of HIRDLS DT frequencies (colored contours) from the Level 2 data and GEOS-5 zonal mean wind on the 200 hPa pressure surface (black contours) versus latitude from 2005 to 2007. Zonal wind contours are 10 m/s, 20 m/s, 30 m/s and 40 m/s.

shift of DT frequencies in the Northern Hemisphere is almost twice as large as the shift in the Southern Hemisphere. In the Northern Hemisphere DT frequencies are highest in 2005 and 2006 and in the Southern Hemisphere DT frequencies are highest in 2006. These variations are, in general, also seen in Figure 5. However, Figure 6 does not capture all of the features seen in Figure 5, such as the increase in DT frequencies in the winter of 2006 relative to 2005. Since the reason for this increase is not apparent in the zonal average the longitude-time structure is examined.

[33] Before using the HIRDLS gridded data on a larger scale, the thermal tropopause definition was applied to a subset of that data and compared well to results from the original (nongridded) data. Gridded temperature data at 12 Coordinated Universal Time (UTC), generated using both the ascending and descending orbit in the observational data set, is used in this analysis. The gridded data was also analyzed at 00:00 UTC (not shown) and confirms the below findings. Additionally, Hovmöller diagrams were produced with both the gridded and original HIRDLS data sets and showed the same structure. However, the HIRDLS Gridded data set is still used since it provides a spatial and temporal continuity not available in the raw satellite observations and does not remove any of the structure found with the raw data.

[34] Hovmöller diagrams, shown in Figure 7, are created for each hemisphere and for all three years. These contour plots are generated by placing midlatitude (25°–55°) DT data from the gridded data set into 15° longitude bins. In Figure 7, Northern Hemisphere DT frequencies are largest in 2006, supporting Figure 5, and maximize between 180° to 360° longitude (the Pacific and Atlantic Oceans) for all three years, corroborating the structure found in Figures 2 and 3. In the Southern Hemisphere DT frequency values decrease, relative to the Northern Hemisphere, do not indicate preferred regions of DT development and seem to propagate beyond the winter/spring season. In the Northern Hemisphere the only visible summer feature occurs between 0° and 90° longitude, which could represent the Asian monsoon, as mentioned in relation to Figures 2 and 3. Regardless of DT strength or region of formation the development, advection and dissipation of this structure can be seen in all six plots. Hovmöller diagrams were also generated using ERA-Interim data (not shown) and were found to agree very well with Figure 7, both in structure and magnitude.

[35] The speed of the features in Figure 7 are found by calculating their slopes using equations (B1) and (B2) (see Appendix B.1 for details). Results from this calculation are represented in each graph with a black dotted line. The slope of the line represents a feature moving eastward at a speed of approximately 18 m/s for the Northern Hemisphere and approximately 22 m/s for the Southern Hemisphere. The pattern and movement of these DT features in the Hovmöller diagram indicate that they have a westward group speed and phase speed relative to the background flow. Therefore, even though the DT is not a Rossby wave itself the advection of the structure is reminiscent of Rossby waves. The previously stated Northern Hemisphere speed is placed into the Rossby Wave dispersion equation (equations (B3) and (B4) in Appendix B.2) and is found to correspond to a wave with a wave number of about 2 and a period of about 10 days, which is visually consistent with Figure 7. In the Southern Hemisphere the wave has a wave number of ∼2.4 with a period of about 7.5 days. Additionally, the duration of the stronger DT structures are estimated using the black dots and are found to vary between 3 and 12 days. In both hemispheres this black dotted line is steeper than the blue line, thus DTs are propagating at speeds that are less than the daily zonal wind speed at 200 hPa.

5. Discussion

[36] The results presented in this study highlight a clear zonal structure in the midlatitude DT occurrence frequency, the DT interannual variability and advection characteristics of the DT structure. Implications of each result and comparisons to previous or related work are discussed below.

[37] In general, seasonal variations in the DT spatial pattern shown in Figure 2 qualitatively agree with previous studies [*Schmidt et al.*, 2006; *Randel et al.*, 2007; *Añel et al.*, 2008]. However, there are slight differences between this

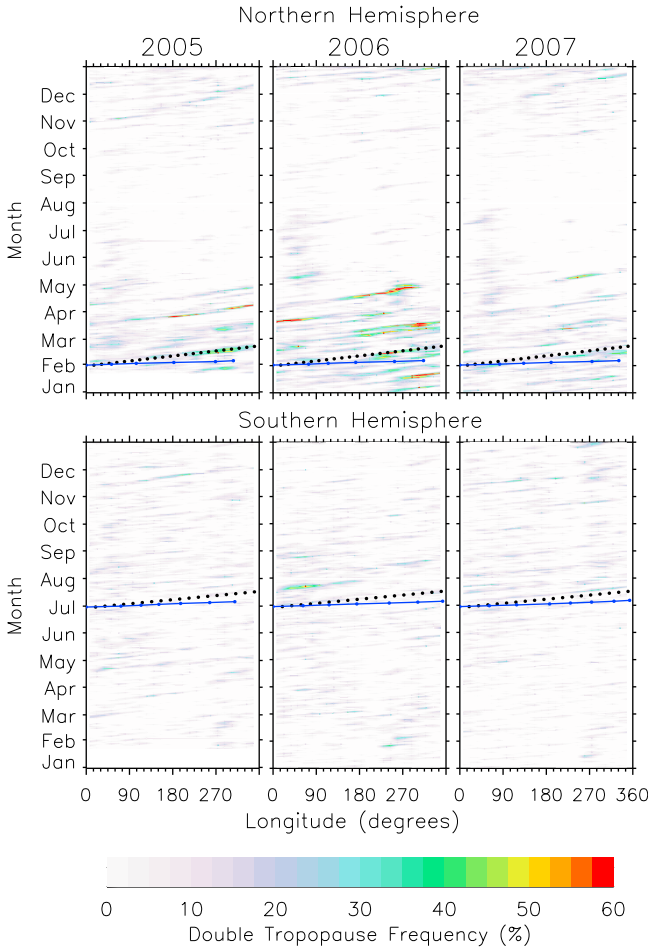

Figure 7. Hovmöller diagrams of HIRDLS DT frequencies generated using the HIRDLS Gridded data set. DT information is gathered between 25° and 55° latitude and then placed into15° longitude bins. Three years are shown, (left) 2005, (middle) 2006, and (right) 2007, for each hemisphere, (top) Northern Hemisphere and (bottom) Southern Hemisphere. The black dotted line represents the slope, thus the speed, of the double tropopause structures. The blue solid line, with blue dots, represents the slope, thus speed, of the GEOS-5 zonal wind at 200 hPa.

study and these other studies, specifically during DJF in the Northern Hemisphere over the Pacific and Atlantic Ocean (called "breaks" in section 4.1), the U.S., and China. Those previous studies [*Schmidt et al.*, 2006; *Randel et al.*, 2007; *Añel et al.*, 2008] showed either the 'break' over the Pacific or Atlantic, but not both. Additionally, only one of the above mentioned studies, *Randel et al.* [2007], found the same Southwest-Northeast tilt in the maximum DT frequencies over the U.S. shown in Figure 2. To better understand these differences Figure 2 was regenerated but with the bins used by *Randel et al.* [2007] and *Añel et al.* [2008] (see Table 1). This figure (not shown), when compared to previous work, agreed less in the Northern Hemisphere and stayed about the same in the Southern Hemisphere, which suggests that bin size alone is not the reason for the presented differences.

[38] Other explanations for discrepancies between this study and previous studies that used observations include the vertical resolution, measurement period, and daily data density (see Table 1). Vertical resolution is very similar between all the above mentioned studies and thus is not a likely explanation for the discrepancies. However, the measurement period could be a reason since none of the studies listed in Table 1 fully overlap with the HIRDLS measurement period. Additionally, HIRDLS data density is very high, about 400 profiles per 3° × 15° bin, and approximately constant across the globe except very close to the polar edges of the instruments latitude range where the orbit track shifts from North-South to East-West. As a result, HIRDLS has the ability to obtain high resolution measurements of the North-South extent of the DT and, consequently, can capture new features. This may explain why the tilt in DT frequencies over the U.S., and their subsequent extension across the Atlantic Ocean, is visible with HIRDLS and not with the data sets shown in Table 1. Last, *Añel et al.* [2008] shows a significant drop in DT frequencies over China, a result that disagrees with other studies. These low values occur over a region with no radiosonde stations within S187, a subset of the S188 Integrated Global Radiosonde Archive (IGRA) data set [*Añel et al.*, 2007], and therefore is the likely cause of the discrepancy.

[39] Only one of the authors in Table 1, *Schmidt et al.* [2006], produced a global plot of DT thickness like Figure 3. In that work the DT thickness follows, quite closely, the DT frequency pattern, which is very different from what is shown in Figure 3. This pattern could be occurring because the retrieval algorithm used in that study set the height of the second tropopause equal to that of the first tropopause if no second tropopause could be determined (T. Schmidt, personal communication, 2011). As a result, regions that contain very few DTs would correspond to regions of low DT thickness since the average calculation would be skewed toward the lower/zero values seeing that they are the majority.

[40] The DT patterns shown in Figures 2 and 3 highlight preferred regions of DT formation during the winters of both the Northern and Southern Hemisphere. Most of these regions, such as the eastern United States, eastern Canada, the northern part of the Pacific Ocean, over Japan, and over the southern half of Australia, are spatially coincide with other atmospheric features such as storm tracks [*Holton*,

Table 1. Properties and Characteristics of Data Set(s) Used For This Study and in Previous DT Studies

Data Set	Time Frame of Data	Vertical Resolution	Horizontal Bins (lat × lon)	Data Density per Day
		Schmidt et al. [2006]		
CHAMP	2001–2005	>1 km	10° × 15°	~150 – 200 soundings
SAC-C	2001–2002	>1 km	10° × 15°	~150 – 200 soundings
		Randel et al. [2007]		
CHAMP	2001–2005	>1 km	10° × 30°	~150 – 200 soundings
SAC-C	2001–2002	>1 km	10° × 30°	~150 – 200 soundings
ERA-40	1957–2002	~1 km		~480 per forecast time
		Añel et al. [2008]		
IGRA S187	1965–2004	~0.5 km	10° × 30°	~374 profiles
		This Study		
HIRDLS	2005–2008	1 km	3° × 15°	~5500 profiles

2004], enhanced synoptic activity [*Añel et al.*, 2008], and regions of tropopause folds [*Elbern et al.*, 1998]. Even though these spatial relationships are somewhat expected, when considering work by *Shapiro* [1978, 1980] and *Bischoff et al.* [2007], areas of weak agreement over Europe and directly over the Andes mountain range suggest that other independent or quasi-independent mechanisms may also be responsible for the formation of DTs.

[41] Another mechanism, which has been examined by both *Pan et al.* [2009] and *Homeyer et al.* [2011] during the winter/spring, include Rossby wave breaking. Even though wave breaking does occur in both hemispheres only the Northern Hemisphere will be discussed since there are no case studies in the Southern Hemisphere that explicitly connect the DT to Rossby wave breaking. During DJF season there are two regions of decreased DT frequency over the eastern Pacific and central Atlantic oceans that correspond to areas of weak zonal flow and diffluence [*Nakamura*, 1994], or a spreading of the streamlines. This wind structure produces regions of poleward wave breaking [*Peters and Waugh*, 1996]. *Homeyer et al.* [2010] examined the evolution of a tropospheric intrusion in both the central Pacific and Atlantic and found that the upper tropopause of the tropospheric intrusion, i.e., a DT, extends poleward and then separated from its tropical reservoir during large amplitude wave breaking. This spatial relationship between the seasonal mean zonal wind structure and DTs, in addition to the large poleward reach of DT thicknesses (strongest in the Pacific Ocean) during DJF, indicates that the Pacific Ocean may be a region of frequent DT formation. However, further analysis is needed since other atmospheric structures could be contributing to the patterns seen in Figures 2, 3, and 7.

[42] In the Northern Hemisphere during JJA, see Figures 2 and 3, there is a region of prominent DT frequencies and thicknesses located over the poleward flank of the Asian monsoon anticyclone. Previous studies have shown a similar feature, but with less horizontal extent either in longitude [*Schmidt et al.*, 2006] or in both longitude and latitude [*Randel et al.*, 2007]. (*Añel et al.* [2008] is not able to capture this feature due to the spatial distribution of the radiosonde stations.). *Randel et al.* [2007] found that DTs which form poleward of the Asian monsoon anticyclone have a dynamical structure that is similar to what is seen in the midlatitudes and that the strong anticyclone contains a relatively high tropical tropopause that can have a large latitudinal extent.

[43] Another region of high DT activity, both in frequencies and thicknesses, occurs over the Southern Hemisphere year round. This prominent feature is over the southern tip of South America and has been seen in previous studies [*Schmidt et al.*, 2006; *Randel et al.*, 2007; *Añel et al.*, 2008], but only for DJF and JJA. *Bischoff et al.* [2007] found the same pattern when examining data from three different rawinsonde stations, finding that two of three stations showed no seasonality, and also found the passage of an intense cold front led to a single-to-double tropopause change in the thermal profile. Another mechanism for the generation of DTs over South America suggested by *Schmidt et al.* [2006] is topography, specifically the Andes Mountains. Over this area mountain waves, a type of gravity wave [*de la Torre et al.*, 2006], are generated from a symmetric and fast zonal wind that varies little from season to season [*Holton*, 2004]. A recent study by *Smith et al.* [2008] found that during strong wave events a layer of strong static stability formed right above the tropopause, with weaker stability above and below, resulting in a strong "tropopause inversion." This strong inversion could support the formation of a DT since such a relationship has been shown when examining baroclinic life cycles [*Wang and Polvani*, 2011]. Even though the six case studies were over the Sierra Nevada range in California, and not the Andes, it is an example of how strong gravity waves, which occur frequently over the Andes [*Alexander et al.*, 2008; *Yan et al.*, 2010], could perturb the tropopause and promote the generation of a DT. This argument does not confirm such a connection, but does suggest the possibility and promotes further investigation of the dynamical and meteorological situation over the Andes Mountains in relation to DTs.

[44] Overall, Figure 4 does verify the general increase of DT thickness with latitude and the corresponding seasonal variation seen in Figure 3. Additionally, Figure 4 highlights the tendency for the single tropopause to lie in between the first and second tropopause of the DT for all four seasons. This relationship is probably due to cyclonic circulations, which are favorable conditions for DT formation [*Randel et al.*, 2007], since that type of horizontal circulation alters the vertical structure by decreasing the altitude of the thermal tropopause up to 2 km [*Wirth*, 2001]. Additionally, the thickness range presented in the results section agrees well with work by *Añel et al.* [2008] and *Randel et al.* [2007]. This good agreement between HIRDLS and radiosonde data [*Añel et al.*, 2008] highlights the effectiveness of HIRDLS in studying the single and double tropopause.

[45] The representation of DT daily frequencies shown in Figure 5 reveal some interesting interannual variability such as the increase in DT frequency during 2006 in both hemispheres. A recent study by *Homeyer et al.* [2011] also found a similar increase in tropospheric intrusions, which form a DT, in the eastern Pacific during 2008, a La Niña year. The author suggested that the increase in intrusions could be due to the Pacific westerly duct (see wind contours in Figures 2 and 3), a tropical upper troposphere mean westerly wind that favors cross-equatorial propagation of Rossby waves, since it is stronger during La Niña/El Niño–Southern Oscillation (ENSO) cold phase. These conditions are also present during 2005 and persisted until the spring of 2006, the same time frame in which HIRDLS shows an increase in DT frequency for the Northern Hemisphere. However, this same relationship is not clear in the Southern Hemisphere since the increase in DT frequency in the winter/spring (June–September) of 2006 occurs during the El Niño conditions or ENSO warm phase. Even though the westerly ducts have been shown to contribute to DT formation work that expands upon case studies is required to fully understanding how atmospheric oscillations may contribute to the DT interannual variability shown in Figure 5.

[46] The daily longitudinal variation of these DT structures are shown in Hovmöller diagrams, see Figure 7, which highlights the movement of the DT structure and its likely connected to Rossby wave propagation and breaking. In the Northern Hemisphere there is high a frequency of occurrence for DTs from the Pacific Ocean to the western edge of

Europe. This region, also noted in Figures 2 and 3, coincides with regions of Rossby wave breaking. Additionally, the low activity over Europe is clearly visible in Figure 7 when it was not in Figure 2, further supporting the idea that enhanced DT activity is isolated to specific regions over the globe. The slopes of these structures result in a speed that is less than the speed of the jet stream in both hemispheres, which indicates that they have a group speed and phase speed that are both westward relative to the mean flow. This is indicative of a Rossby wave, which is an idea that has been suggested in this manuscript and recently by *Castanheira and Gimeno* [2011]. Therefore, the interannual variability shown in Figures 5, 6, and 7, along with the preferred regions of formation shown in Figure 7, support a connection between DTs and Rossby waves along with potential for Rossby waves to play a role in the development of the DT. Moreover, these features propagate at speeds that are between the minimum and maximum mean zonal wind speeds at 300 hPa [*Randel and Held*, 1991], which suggests that the waves could be baroclinic in nature [*Randel and Held*, 1991; *Holton*, 2004].

6. Conclusions

[47] The tropopause is a key feature in the UTLS region since it separates radiately important constituents, that, if redistributed irreversibly, could change the Earth's radiation budget and alter the surface climate [*Forster and Shine*, 1997; *Solomon et al.*, 2010]. Previous UTLS studies have shown a relationship between Rossby waves and the formation of a second tropopause, i.e., double tropopause, above the subtropical jet [*Castanheira and Gimeno*, 2011; *Homeyer et al.*, 2011; *Pan et al.*, 2009; *Randel et al.*, 2007], highlighting the potential importance of the DT for the UTLS region. This study supports that relationship and expands upon it by placing it in a larger context using 3 years of high density, high resolution near-global satellite data from HIRDLS.

[48] The primary findings are as follows.

[49] 1. Clear zonal structure in the DT frequency of occurrence (see Figure 2) during DJF that coincides with breaks in the seasonal mean zonal wind and regions of known poleward wave breaking.

[50] 2. DTs are found to form over the southern tip of South America for all seasons and are connected to gravity waves originating from the Andes using other recent studies.

[51] 3. DT thickness and frequency patterns have a similar spatial structure. Deviations in thickness occur poleward of the subtropical jet over the Pacific Ocean, in both hemispheres, and poleward of eastern Australia in the Southern Hemisphere, all regions of poleward wave breaking.

[52] 4. The presence of DT activity poleward of the Asian anticyclone, during JJA.

[53] 5. Statistically significant interannual variability in the Northern Hemisphere between 2007 and the other two years, 2005 and 2006.

[54] 6. Formation of the DT at and poleward of the subtropical jet found to be consistent over all three years, 2005–2007, and for both hemispheres.

[55] 7. Evidence of Rossby wave characteristics in Hovmöller diagram of DT frequencies. Application of the Rossby wave dispersion relation found that the patterns correspond to waves with the following properties for the Northern and Southern Hemisphere, respectively: wave number = 2 and period = 10 days, wave number = 2.4 and period = 7.5 days.

Appendix A: Basic Logic of Double Tropopause Search Algorithm

[56] The IDL code for the program is not included since the algorithm developed to find the thermal tropopause does not use any unique techniques. However, the basic steps for developing a similar algorithm are shown below.

[57] 1. Calculate the lapse rate γ (defined as $-dT/dz$) for the selected profile between 5 km or ~550 hPa (to avoid interference from surface inversions) and 20 km (since the maximum height for the tropopause is ~17 km).

[58] 2. Find where the lapse rate is first equal to or below 2 °C/km, then calculate the average lapse rate value between that level and 2 km above that level.

[59] 3. If the average lapse rate is equal to or less than 2°C/km then you have found the first tropopause and should continue with the below steps, otherwise move on to the next vertical profile and return to step 1.

[60] 4. Save this point, the altitude of the first tropopause, in an array. If available save the pressure, temperature, etc., information of the first tropopause also.

[61] 5. Above the first tropopause look for the average lapse rate to exceed 3°C/km for 1 km. Note that this 1 km range may include one or many altitude levels, therefore, mark or save the lowest level at which the criteria is satisfied.

[62] 6. If the average lapse rate is greater than 3°C/km then you will continue the search for the second tropopause by moving on to the next step (step 7), otherwise move on to the next vertical profile and return to step 1.

[63] 7. The second tropopause can be within or above the altitude level found in the previous step (step 6), so search for the second tropopause above that level by repeating steps 2, 3, and 4.

[64] 8. If the average lapse rate is equal to or less than 2°C/km then you have found the second tropopause and should save the altitude and pressure information. Now move on to the next profiles and start the search over by returning to step 1.

Appendix B: Hovmöller Diagram Calculations

B1. Black Dotted Line

[65] The black sloped line in Figure 7 is calculated using the arc length formula

$$s = \varphi r, \tag{B1}$$

where φ equals the longitude, s the arc length, and r the radius of the object. Here the object is on the Earth, therefore $r = R\cos(\theta)$ with R = 6,378,000.0 meters (the radius of the Earth) and $\theta = 30°$ latitude. This latitude is chosen since DTs form over the subtropical jet, which is located at approximately 30° latitude during the winter of both hemispheres [*Holton*, 2004]. The arc length, or s, is equivalent to distance, which is approximated using the Newtonian speed × time

calculation. The variable of interest is the speed (U). This is found by rearranging s so that $U = s/T$, where the time (T) is estimated to equal the passage of approximately 22 days (found using Figure 7) and the distance (s) is equal to equation (B1). The time (T) is adjusted until the correct slope for the black-dotted line is found through visual verification. Now formula (B1) is

$$U = \frac{\varphi R \cos\theta}{T}. \quad \text{(B2)}$$

[66] The distance traveled over the time period T is given by $\varphi R\cos\theta$ where φ is converted from 360 degrees to $\pi/180$ radians. This is done for each hemisphere since it is clear, visually, that U is not the same in both hemispheres. Using both of the above equations the speed of DT features in the Northern Hemisphere is found to be 18 m/s and 22 m/s in the Southern Hemisphere. After U is found for each hemisphere the black-dotted line is generated, with each dot representing the passage of 1 day. Consequently, these black dots can be used to estimate the duration of prominent features. The same formulas are used to generate the blue solid-dotted line in Figure 7, with one difference. For that line the wind variable (U) is not set to a constant value, instead it is the maximum GEOS5 zonal wind value on the 200 hPa surface. Therefore, as the wind varies from day to day, so does the distance traveled each day and thus the distance between each blue dot is not constant.

B2. Wave Number and Period

[67] For this calculation the group speed formulation of the Rossby wave dispersion equation (B3) is used to calculate the zonal wave number and, from there, the corresponding the planetary zonal wave number and period.

$$c_g \equiv \frac{\partial w}{\partial k} = U - \frac{\beta(\ell^2 - k^2)}{(k^2 + \ell^2)^2}. \quad \text{(B3)}$$

In this formula U is equal to the mean westerly flow, k and l represent the zonal and meridional wave numbers, ω is equal to the angular speed of the Earth (7.292×10^{-5} radians per second), and β is the Rossby parameter, $[2\omega\cos(\theta)]/R$. From Figure 7 it is clear that $c_g < U$ for both hemispheres and, therefore, these are probably long Rossby waves, i.e., $l > k$. To test how sensitive the zonal wave number is to changes in the meridional wave number l is replaced with nk. After considering these additions equation (B3) changes to

$$c_g \equiv \frac{\partial \omega}{\partial k} = U - \frac{\beta(n^2 - 1)}{k^2(1 + n^2)^2}, \quad \text{(B4)}$$

where $n > 1$.

[68] During the Northern Hemisphere winter, the zonal wind speed (U) is taken to be 35 m/s and the approximate location of the subtropical jet is 30° latitude (θ). These are approximate values and are chosen through a visual inspection of the location of maximum DT frequency in Figure 6. Inserting these values into formula (B4) the group speed from Appendix B.1, 18 m/s, is also placed into formula (B4) and solved for k, which is in units of inverse meter. Once k is known two formulas are needed to find the planetary zonal wave number and the corresponding period, $s = Lk/2\pi$ and $t = 2\pi/(c_g{*}k)$, respectively, with L = circumference of the Earth at a specific latitude. If $n = 2$ the DT features in the Northern Hemisphere, which have been shown to move at ~18 m/s, correspond to a wave of ~wave number 2 with a period of ~10 days. In the Southern Hemisphere c_g = 22 m/s, which corresponds to a wave of ~wave number 2.4 with a period of ~7.5 days. Even though these wave numbers are visually consistent with Figure 7 they would result in large meridional wave numbers based on $l = nk$. Therefore, the sensitivity of planetary zonal wave number and period to changes in n, θ, and U were tested. These tests found that if θ and U are decreased then s increases and t decreases, with the planetary zonal wave number ranging between 0 and ~6. Additionally, if θ and U are fixed to the previously mentioned values and n is increased s will also increase, approaching $s = 3$, until $n = 2$. When n is greater than two s begins decreasing, approaching the limit $s = 0$. Therefore, in equation (B4), the range of s depends much more on θ and U then it does on n. This result is by no means complete, but does give some added insight into Figure 7 and constitutes the first step in a more robust analysis.

[69] **Acknowledgments.** The work discussed in this paper is funded by NASA's AURA satellite program under contract NAS5–97046. The authors would like to thank the HIRDLS Team for access to the data and their support of this work. Special thanks go to Bill Randel and Laura Pan for valuable discussions on the complexities of the extratropical UTLS.

References

Alexander, M. J., et al. (2008), Global estimates of gravity wave momentum flux from High Resolution Dynamics Limb Sounder observations, *J. Geophys. Res.*, *113*, D15S18, doi:10.1029/2007JD008807.

Añel, J. A., J. C. Antuña, L. de la Torre, R. Nieto, and L. Gimeno (2007), Global statistics of multiple tropopauses from the IGRA database, *Geophys. Res. Lett.*, *34*, L06709, doi:10.1029/2006GL029224.

Añel, J. A., J. C. Antuña, L. de la Torre, J. M. Castanheira, and L. Gimeno (2008), Climatological features of global multiple tropopause events, *J. Geophys. Res.*, *113*, D00B08, doi:10.1029/2007JD009697.

Barnett, J. J., C. L. Hepplewhite, S. Osprey, J. C. Gille, and R. Khosravi (2008), Cross-validation of HIRDLS and COSMIC radio-occultation retrievals, particularly in relation to fine vertical structure, *Proc. SPIE Int. Soc. Opt. Eng.*, *7082*, 708216, doi:10.1117/12.800702.

Bethan, S., G. Vaughan, and S. J. Reid (1996), A comparison of ozone and thermal tropopause heights and the impact of tropopause definition on quantifying the ozone content on the troposphere, *Q. J. R. Meteorol. Soc.*, *122*, 929–944, doi:10.1002/qj.49712253207.

Birner, T. (2006), Fine-scale structure of the extratropical tropopause region, *J. Geophys. Res.*, *111*, D04104, doi:10.1029/2005JD006301.

Birner, T., A. Dörnbrack, and U. Schumann (2002), How sharp is the tropopause at midlatitudes?, *Geophys. Res. Lett.*, *29*(14), 1700, doi:10.1029/2002GL015142.

Bischoff, S. A., P. O. Canziani, and A. E. Yuchechen (2007), The tropopause at southern extratropical latitudes: Argentine operational rawinsonde climatology, *Int. J. Climatol.*, *27*, 189–209, doi:10.1002/joc.1385.

Castanheira, J. M., and L. Gimeno (2011), Association of double tropopause events with baroclinic waves, *J. Geophys. Res.*, *116*, D19113, doi:10.1029/2011JD016163.

de la Torre, A., P. Alexander, P. Llamedo, C. Menéndez, T. Schmidt, and J. Wickert (2006), Gravity waves above the Andes detected from GPS radio occultation temperature profiles: Jet mechanism?, *Geophys. Res. Lett.*, *33*, L24810, doi:10.1029/2006GL027343.

Elbern, H., J. Hendricks, and A. Ebel (1998), A climatology of tropopause folds by global analyses, *Theor. Appl. Climatol.*, *59*, 181–200, doi:10.1007/s007040050023.

Forster, P. M. F., and K. P. Shine (1997), Radiative forcing and temperature trends from stratospheric ozone changes, *J. Geophys. Res.*, *102*(D9), 10,841–10,855, doi:10.1029/96JD03510.

Gille, J. C., and J. J. Barnett (2010), High Resolution Dynamics Limb Sounder Earth Observing System (EOS) data description and quality, report, 63 pp., Dep. of Atmos. Oceanic and Planet. Phys., Oxford Univ., Oxford, U. K. [Available at http://www.eos.ucar.edu/hirdls/data/products/HIRDLS-V5-DQD.pdf.]

Gille, J. C., and L. J. Gray (2011), High Resolution Dynamics Limb Sounder Earth Observing System (EOS) data description and quality, report, 103 pp., Dep. of Atmos. Oceanic and Planet. Phys., Oxford Univ., Oxford, U.K. [Available at http://www.eos.ucar.edu/hirdls/data/products/HIRDLS-DQD_V6-1.pdf.]

Gille, J. C., et al. (2008), The High Resolution Dynamics Limb Sounder (HIRDLS): Experiment overview, recovery, and validation of initial temperature data, *J. Geophys. Res.*, *113*, D16S43, doi:10.1029/2007JD008824.

Hoinka, K. P. (1997), The tropopause: Discovery, definition and demarcation, *Z. Meteorol.*, *6*, 281–303.

Holton, J. R. (2004), *An Introduction to Dynamic Meteorology*, 4th ed., 535 pp., Academic, Burlington, Mass.

Holton, J. R., P. Haynes, M. McIntyre, A. Douglass, R. Rood, and L. Pfister (1995), Stratosphere-troposphere exchange, *Rev. Geophys.*, *33*(4), 403–439, doi:10.1029/95RG02097.

Homeyer, C. R., K. P. Bowman, and L. L. Pan (2010), Extratropical tropopause transition layer characteristics using high-resolution sounding data, *J. Geophys. Res.*, *115*, D13108, doi:10.1029/2009JD013664.

Homeyer, C. R., K. P. Bowman, L. L. Pan, E. L. Atlas, R. Gao, and T. L. Campos (2011), Dynamical and chemical characteristics of tropospheric intrusions observed during START08, *J. Geophys. Res.*, *116*, D06111, doi:10.1029/2010JD015098

Hoskins, B. J., M. E. McIntyre, and A. W. Robertson (1985), On the use and significance of isentropic potential vorticity maps, *Q. J. R. Meteorol. Soc.*, *111*, 877–946, doi:10.1256/smsqj.47001.

Keyser, D., and M. A. Shapiro (1986), A review of the structure and dynamics of upper-level frontal zones, *Mon. Weather Rev.*, *114*, 452–499, doi:10.1175/1520-0493(1986)114<0452:AROTSA>2.0.CO;2.

Khosravi, R., et al. (2009), Overview and characterization of retrievals of temperature, pressure, and atmospheric constituents from the High Resolution Dynamic Limb Sounder (HIRDLS) measurements, *J. Geophys. Res.*, *114*, D20304, doi:10.1029/2009JD011937.

Kochanski, A. (1955), Cross sections of the mean zonal flow and temperature along 80°W, *J. Meteorol.*, *12*, 95–106, doi:10.1175/1520-0469(1955)012<0095:CSOTMZ>2.0.CO;2.

Kohri, W. J. (1981), LRIR observations of the structure and propagation of stationary planetary waves in the Northern Hemisphere during December 1975, Ph.D. dissertation, Drexel Univ., Philadelphia, Pa.

Kunz, A., P. Konopka, R. Müller, and L. L. Pan (2011), The dynamical tropopause based on isentropic potential vorticity, gradients, *J. Geophys. Res.*, *116*, D01110, doi:10.1029/2010JD014343.

Lahoz, W. A., S. A. Buehler, and B. Legras (2007), The COST 723 action, *Q. J. R. Meteorol. Soc.*, *133*, 99–108, doi:10.1002/qj.158.

Nakamura, M. (1994), Characteristics of potential vorticity mixing by breaking Rossby waves in the vicinity of the jet, D.Sc. thesis, 253 pp., Mass. Inst. of Technol., Cambridge, Mass.

Noerdlinger, P. D., and L. Klein (1995), Theoretical basis of the SDP toolkit geolocation package for the ECS project, *Tech. Pap. 445-TP-002–002*, 203 pp., Hughes Appl. Info. Syst., Landover, Md., 18 May.

Olsen, M. A., A. R. Douglass, M. R. Schoeberl, J. M. Rodriquez, and Y. Yoshida (2010), Interannual variability of ozone in the winter lower stratosphere and the relationship to lamina and irreversible transport, *J. Geophys. Res.*, *115*, D15305, doi:10.1029/2009JD013004.

Pan, L. L., and L. A. Munchak (2011), Relationship of cloud top to the tropopause and jet structure from CALIPSO data, *J. Geophys. Res.*, *116*, D12201, doi:10.1029/2010JD015462.

Pan, L. L., W. J. Randall, B. L. Gary, M. J. Mahoney, and E. J. Hintsa (2004), Definitions and sharpness of the extratropical tropopause: A trace gas perspective, *J. Geophys. Res.*, *109*, D23103, doi:10.1029/2004JD004982.

Pan, L. L., W. J. Randel, J. C. Gille, W. D. Hall, B. Nardi, S. Massie, V. Yudin, R. Khosravi, P. Konopka, and D. Tarasick (2009), Tropospheric intrusions associated with the secondary tropopause, *J. Geophys. Res.*, *114*, D10302, doi:10.1029/2008JD011374.

Peters, D., and D. W. Waugh (1996), Influence of barotropic shear on the poleward advection of upper tropospheric air, *J. Atmos. Sci.*, *53*, 3013–3031, doi:10.1175/1520-0469(1996)053<3013:IOBSOT>2.0.CO;2.

Peters, D., and D. W. Waugh (2003), Rossby wave breaking in the Southern Hemisphere wintertime upper troposphere, *Mon. Weather Rev.*, *131*, 2623–2634, doi:10.1175/1520-0493(2003)131<2623:RWBITS>2.0.CO;2.

Randel, W. J., and I. M. Held (1991), Phase speed spectra of transient Eddy fluxes and critical layer absorption, *J. Atmos. Sci.*, *48*, 688–697, doi:10.1175/1520-0469(1991)048<0688:PSSOTE>2.0.CO;2.

Randel, W. J., D. J. Seidel, and L. L. Pan (2007), Observational characteristics of double tropopauses, *J. Geophys. Res.*, *112*, D07309, doi:10.1029/2006JD007904.

Remsberg, E. E., K. V. Haggard, and J. M. Russell (1990), Estimation of synoptic fields of middle atmosphere parameters from Nimus-7 LIMS profiles data, *J. Atmos. Ocean Sci.*, *7*, 689–705.

Rienecker, M. M., et al. (2008), The GEOS-5 data assimilation system—Documentation of versions 5.0.1, 5.1.0, and 5.2.0, *NASA Tech. Memo.*, vol. 27, 97 pp.

Rodgers, C. D. (1976), Retrieval of atmospheric temperature and composition from remote measurements of thermal radiation, *Rev. Geophys.*, *14*, 609–624, doi:10.1029/RG014i004p00609.

Rodgers, C. D. (2000), *Inverse Methods for Atmospheric Sounding: Theory and Practice*, World Sci., Singapore.

Schmidt, T., G. Beyerle, S. Heise, J. Wickert, and M. Rothacher (2006), A climatology of multiple tropopauses derived from GPS radio occultations with CHAMP and SAC-C, *Geophys. Res. Lett.*, *33*, L04808, doi:10.1029/2005GL024600.

Seidel, D., and W. J. Randel (2006), Variability and trends in the global tropopause estimated from radiosonde data, *J. Geophys. Res.*, *111*, D21101, doi:10.1029/2006JD007363.

Shapiro, M. A. (1978), Further evidence of the mesoscale and turbulent structure of upper level jet stream-frontal zone systems, *Mon. Weather Rev.*, *106*, 1100–1111, doi:10.1175/1520-0493(1978)106<1100:FEOTMA>2.0.CO;2.

Shapiro, M. A. (1980), Turbulent mixing within tropopause folds as a mechanism for exchange of chemical constituents between the stratosphere and troposphere, *J. Atmos. Sci.*, *37*, 994–1004, doi:10.1175/1520-0469(1980)037<0994:TMWTFA>2.0.CO;2.

Smith, R. B., B. K. Woods, J. Jensen, W. A. Cooper, J. D. Doyle, Q. Jiang, and V. Grubisic (2008), Mountain waves entering the stratosphere, *J. Atmos. Sci.*, *65*, 2543–2562, doi:10.1175/2007JAS2598.1.

Solomon, S., K. H. Rosenlof, R. W. Portmann, J. S. Daniel, S. M. Davis, T. J. Sanford, and G.-K. Plattner (2010), Contributions of stratospheric water vapor to decadal changes in the rate of global warming, *Science*, *327*(5970), 1219–1223, doi:10.1126/science.1182488.

Wang, S., and L. M. Polvani (2011), Double tropopause formation in idealized baroclinic life cycles: The key role of an initial tropopause inversion layer, *J. Geophys. Res.*, *116*, D05108, doi:10.1029/2010JD015118.

Wirth, V. (2001), Cyclone-anticyclone asymmetry concerning the height of the thermal and the dynamical tropopause, *J. Atmos. Sci.*, *58*, 26–37, doi:10.1175/1520-0469(2001)058<0026:CAACTH>2.0.CO;2.

World Meteorological Organization (1957), Meteorology—A three-dimensional science: Second session of the commission for aerology, *WMO Bulletin*, *4*(4), 134–138.

Wright, C. J., M. B. Rivas, and J. C. Gille (2011), Intercomparisons of HIRDLS, COSMIC and SABER for the detection of stratospheric gravity waves, *Atmos. Meas. Tech.*, *4*, 1581–1591, doi:10.5194/amt-4-1581-2011.

Yan, X., N. Arnold, and J. Remedios (2010), Global observations of gravity waves from High Resolution Dynamics Limb Sounder temperature measurements: A yearlong record of temperature amplitude and vertical wavelength, *J. Geophys. Res.*, *115*, D10113, doi:10.1029/2008JD011511.

Zängl, G., and K. P. Hoinka (2001), The tropopause in the polar regions, *J. Clim.*, *14*, 3117–3139, doi:10.1175/1520-0442(2001)014<3117:TTITPR>2.0.CO;2.

J. C. Gille, Center for Limb Atmospheric Sounding, University of Colorado at Boulder, PO Box 3000, Boulder, CO 80307-3000, USA.

A. Kunz, Institute for Energy and Climate Research, IEK-7: Stratosphare, Forschungszentrum Jülich, ICG-1, Wilhem-Jonen Strasse, D-52425 Jülich, Germany.

T. R. Peevey, Department of Atmospheric and Oceanic Sciences, University of Colorado at Boulder, 311 UCB Folsom Stadium, Rm 255, Gate 7, Boulder, CO 80309, USA. (phillitr@colorado.edu)

C. E. Randall, Laboratory for Atmospheric and Space Sciences, University of Colorado at Boulder, UCB 392, Boulder, CO 80309-0392, USA.